THE JOURNAL OF PHYSICAL CHEMISTRY B
A JOURNAL OF THE AMERICAN CHEMICAL SOCIETY

pubs.acs.org/JPCB

Article

Low Interfacial Free Energy Describes the Bulk Ordering Transition in Colloidal Cubes

Published as part of The Journal of Physical Chemistry virtual special issue "Carol K. Hall Festschrift".

Abhishek K. Sharma and Fernando A. Escobedo*

Cite This: *J. Phys. Chem. B* 2021, 125, 5160–5170

Read Online

ACCESS | Metrics & More | Article Recommendations | Supporting Information

ABSTRACT: Many hard faceted nanoparticles are known to undergo disorder-to-order phase transitions following a classical nucleation and growth mechanism. In a previous study [*J. Phys. Chem. B* **2018**, *122*, 9264−9273], it was shown that hard cubes undergo a nonclassical phase transition with a bulk character instead of originating from consolidated nuclei. Significantly, an unusually high fraction of ordered particles was observed in the metastable basin of the disordered phase, even for very low degrees of supersaturation. This work aims to substantiate the conjecture that these unique properties originate from a comparatively low interfacial free energy between the disordered and ordered phases for hard cubes relative to other hard particle systems. Using the cleaving wall method to directly measure the interfacial free energy for cubes, it is found that its values are indeed small; e.g., at phase coexistence conditions, it is only one-fifth that for hard spheres. A theoretical nucleation model is used to explore the broader implications of low interfacial tension values and how this could result in a bulk ordering mechanism.

1. INTRODUCTION

Recent advancements in chemical synthesis[1−3] have enabled an unprecedented control of the shape and monodispersity of nanoparticles. Such tailored nanoscale colloids are important as building blocks for bottom-up materials design[4−8] with potential applications in photonics[9] and plasmonics.[10,11] In the absence of strong, ligand- or patch-mediated energetic interactions, the self-assembling properties of colloidal nanoparticles can be largely traced to their shape and have been predicted through "hard" particle models, e.g., the formation of different crystalline structures,[12] and mesophases,[13−17] and the occurrence of phase transitions.[18−24] To date, many of these predictions have been confirmed through experiments.[1,25−29]

Computer simulations have revealed that hard colloidal nanoparticles often undergo first-order, disorder-to-order phase transitions in 3D space.[18,21,22] One of the first cases studied through simulations was that of hard spheres,[30] which form a face-centered cubic (FCC) lattice via nucleation and growth.[18,19] Adding anisotropy to the shape of the particle, say by adding facets, alters the phase behavior by favoring ordered structures that enhance packing entropy.[12,13] As for the phase transition kinetics, the faceted particles studied thus far have been found to generally order via nucleation and growth.[21−23,31]

Remarkably, simulations of hard cubic nanoparticles reveal both unusual phase behavior[13,32,33] and ordering kinetics. Upon compression, they form an ordered phase with orientationally aligned particles arranged in a simple cubic lattice. Near the phase transition, this ordered phase has an unusually high diffusivity and concentration of vacancies for a crystalline phase when compared to that for other particle shapes. In a recent study[24] where the disorder-to-order transition of hard cubes was tracked and free energy barriers were mapped via umbrella sampling, we observed that the kinetic pathway toward ordering was also unusual. Unlike most other polyhedra that have been studied in the literature,[21,22] the phase transition in cubes is not well-described by classical nucleation and growth. Instead, it undergoes a "bulk-like" transition behavior with the following features:

I. A large number of sparse, small clusters of ordered particles are present in the disordered phase. The concentration of ordered particles increases with supersaturation and, at a given supersaturation, is much higher

Received: February 25, 2021
Revised: April 20, 2021
Published: May 4, 2021

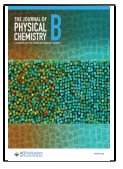

https://doi.org/10.1021/acs.jpcb.1c01737
J. Phys. Chem. B 2021, 125, 5160–5170

when compared to other polyhedra that undergo nucleation and growth.

II. The apparent free energy barrier for the ordering transition was found to scale linearly with system size, which would imply that in a system of macroscopic size the transition would be practically impossible.

III. At no or a minimal degree of supersaturation, a critical concentration of ordered cubes, rather than a critically sized ordered nucleus, needs to be attained for the transition to proceed. During the transition, the fraction of ordered particles gradually increases, leading to consolidation of ordered domains and an eventual transition to the ordered phase.

It is well-established that any stable or metastable phase will exhibit local fluctuations in structural order where motifs associated with another phase may occur.[34] While these fluctuations will largely be transient, they will also encompass the seeds of an incipient (stable) phase as it nucleates and grows within a metastable phase. Of course, such fluctuations also exist in a stable phase, albeit these are fewer and too small to initiate any phase transition. The presence of a significant fraction of ordered particles in a disordered phase reflects the ease of creating interfaces in the system, i.e., a small interfacial free energy between the ordered and disordered phases. Hence, we hypothesize that the abundance of such fluctuations that resemble the ordered phase (henceforth simply referred to as *cubatic fluctuations*) in the disordered phase of the cubes could be attributed to a low surface tension. In this paper, we conduct direct measurements of the interfacial free energy of a disorder−order interface for hard cubes and compare the resulting values to those of other hard-core systems. We also present a mass action-derived classical nucleation theory (MADCNT) model to qualitatively understand how the extent of cubatic fluctuations depends on the interfacial free energy.

The paper is structured as follows: In Section 2, we outline the implementation of the cleaving-walls method in Monte Carlo simulations. In Section 3, we present our results and discuss them in the context of a theoretical model to explore the consequences of low surface tensions on the concentration of cubatic fluctuations. In Section 4, we provide a summary and outlook of our results.

2. METHODS

2.1. Model. For any two cubic particles i and j, we use a hard pair-potential given by

$$U_{ij} = \begin{cases} 0 & \text{if no overlap} \\ \infty & \text{if overlap} \end{cases} \quad (1)$$

The overlap is detected by using the separating axis theorem.[35]

2.2. Monte Carlo Simulations. We use Metropolis[30] Monte Carlo (MC) simulations in either the canonical (NVT) or the isothermal−isobaric (NpT) ensemble as necessary, where N is the total number of particles, V is the volume of the system, p is the pressure, and T is the temperature. We use scaled units consistent with our previous studies,[13] with lengths scaled by the circumradius (a_c) of the polyhedron. Thus, the dimensionless pressure is given by $p = \beta p_a a_c^3$, where p_a is the unscaled pressure and $\beta = \frac{1}{k_B T}$, where k_B is Boltzmann's constant. The chemical potential (μ) and free energy (ΔG) are scaled by $k_B T$, and the dimensionless interfacial free energy is given by $\gamma = \beta \gamma_a a_c^2$ where γ_a is the unscaled interfacial free energy. For a comparison among different particle shapes, we tried to remove the dependence on the choice of length scale a_c, by defining a reduced dimensionless interfacial free energy as $\overline{\gamma} = \frac{\gamma}{\rho_s^{2/3}}$, where ρ_s is the density of the solid/ordered phase. This definition is identical to that in an earlier study,[21] and is consistent with the dimensionless surface component of free energy in classical nucleation theory. The supersaturation is defined as $\Delta\mu_{od} = \mu_o - \mu_d$, where μ_o and μ_d are chemical potentials associated with ordered and disordered phases, respectively. The coexistence pressure p_{co} for hard cubes under this scaling is $p = 4.0$ as reported in the literature.[32] The simulations used periodic boundary conditions to mimic bulk behavior. Each MC cycle included N translation, N rotation, and 2 isotropic volume moves (for NpT ensemble runs only).

2.3. Cleaving-Walls Method. *2.3.1. Outline.* The cleaving-walls method used in this study is a Monte Carlo adaptation of an existing method[36] typically implemented using molecular dynamics simulations. While there have been several modifications of the method over the years[37] to improve accuracy, we use an early, simple implementation which proved to be sufficiently accurate for our purposes. To the best of our knowledge, this is the first implementation of the method using Monte Carlo simulations.

The method involves three steps:

I. Cleaving: Start from independent simulation boxes of the two phases at a given pressure (Figure 1a). The two boxes need to have the same cross-sectional dimensions

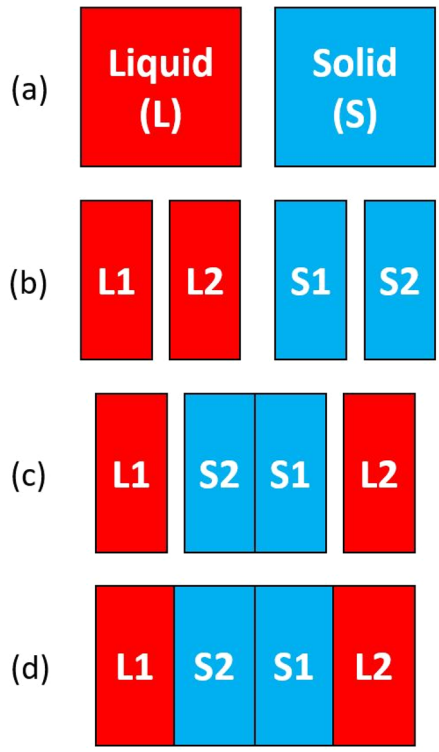

Figure 1. Schematic illustration of steps in the cleaving-walls method. (a) Bulk simulation boxes of solid and liquid phases with three-dimensional periodic boundary conditions at the desired pressure. (b) Phases cleaved at the midplanes. (c) Transposed simulation boxes with dissimilar phases facing each other. (d) Final two-phase state with the gap closed and the two interfaces created.

https://doi.org/10.1021/acs.jpcb.1c01737
J. Phys. Chem. B 2021, 125, 5160−5170

along the cleaving plane and satisfy periodic boundary conditions. Move the cleaving walls to create a gap in the midplane of the simulation box such that particles do not interact across the gap (Figure 1b).

II. Transposition: Rearrange the boxes as shown in Figure 1c to create a larger simulation box with two gaps with dissimilar phases facing each other.

III. Merging: Recede the two pairs of cleaving walls to close the gaps, creating two interfaces (Figure 1d).

The interfacial free energy is then defined as the work done through these steps per unit area of the interface created. Since the interfacial particles do not undergo any change in energy at step II, the interfacial free energy γ is given by the following expression:

$$\gamma = w_{\mathrm{I}} + w_{\mathrm{III}} \tag{2}$$

Here, w_{I} is the work done per unit area on both systems in step I, and w_{III} is the work done per unit area on the transposed system in step III. The latter is negative and smaller in magnitude, resulting in a positive value for γ.

The pressure faced by the cleaving wall is measured throughout steps I and III, and it is crucial to move the wall very gradually to minimize hysteresis. The values were verified by also conducting the process in reverse, i.e., by cleavage of an interface. The initial setup, definition of the cleaving wall, and pressure calculation are described in the next subsections.

2.3.2. Initial Setup. We performed all the calculations at the estimated bulk coexistence pressure $p = 4.0$. As described in previous studies, the ordered phase of hard cubes at coexistence was generated by sequential NpT runs of 3×10^6 MC cycles each, starting from a high pressure ($p = 20$) and gradually reducing the pressure to $p = 4.0$. For the (100) crystal plane, configurations with $N = 1000$ were prepared on a simple cubic lattice aligned with the box vectors of a cubic box. The configurations presenting the (110) crystal plane were obtained in a cuboidal box with $N = 1024$ particles.

To obtain the disordered phase simulation box, the ordered phase simulation box was melted at $p = 1.0$ with anisotropic volume moves along the z-direction (orthogonal to the cleaving plane) to maintain the cross-sectional $(x-y)$ dimensions consistent for transposition in step II. The system was then compressed to $p = 4.0$ to obtain the equilibrium disordered phase at coexistence. To circumvent the finite-size effect of the interfacial region propagating into the bulk-phase structure, longer boxes with $N = 2000$ were primarily studied; these systems were obtained by duplicating the box along the z-direction, followed by equilibration for 3×10^6 MC cycles.

2.3.3. Cleaving Walls. We implemented the cleaving walls as hard planes that only interact with the centroids of the particles (see Supporting Information for discussion on walls that interact with the full particle shapes). There are two walls, one which moves in the $+z$-direction and the other in the $-z$-direction. For a given simulation box, both walls start at the midplane along the z-axis, and particles are disallowed from crossing the midplane or the wall. A given wall only interacts with particles in the direction of its movement during step I. The simulation is conducted in the NVT ensemble, and at the end of each MC cycle, walls are moved in either direction by small increments ($<10^{-4}$, in reduced units) with smaller increments used in cases where a particle would obstruct the wall. For example, if a movement of 10^{-4} would lead to an overlapping particle, a movement of 10^{-5} would be considered. This process is continued until we have achieved a separation of at least one particle circumradius, ensuring that the particles do not interact across the gap. Throughout the process, we output configurations at various separations to perform pressure calculations as described later.

After transposing the two phases with dissimilar phases facing each other across the gaps, the two gaps are closed in small steps corresponding to separations at which the pressure will be calculated ($<10^{-3}$). Each time the separation is reduced, the system is given 10^3 MC cycles to relax. Eventually, the gap is entirely closed, and the system has two interfaces of area equal to the box cross-section.

2.3.4. Pressure and Work Calculation. We calculate the pressure on the wall using virtual perturbations of the wall position following similar well-known volume perturbation methods:[38]

$$p = \left(\frac{\partial F}{\partial V}\right)_{N,T} = \frac{\ln(\langle e^{-\beta \Delta U}\rangle)}{\Delta V} \tag{3}$$

where F is the free energy, V is the volume of box, U is the configurational energy, and the changes $(\Delta U, \Delta V)$ are obtained upon virtual movements of the wall. Let the initial wall position from the midplane be z and the cross-sectional area in the xy plane be A. If the wall is moved by δz, then the change in volume $\Delta V = -A\delta z$, and we can write down eq 3 as

$$p(z) = -\frac{\ln(\langle e^{-\beta \Delta U(z)}\rangle)}{A\delta z} \tag{4}$$

The expression $\langle e^{-\beta \Delta U)} \rangle$ in our case can be interpreted as the ensemble-average probability of overlap between the wall and any particle upon perturbation. For cubes, we generally use $\delta z = 0.001$ (see Supporting Information).

To accurately determine the pressure at a given separation, we conduct an NVT simulation with the initial configurations as described previously. Each simulation was conducted for 10^6 MC cycles, and overlap with a virtual perturbation was checked every 10 cycles. The statistics thus obtained were analyzed to calculate the pressure $p(z)$ for steps I and III. Assuming a reversible process, the work done per unit area was calculated with the following expression that integrates pressure (force per unit area on the plane) over the displacement of the wall:

$$w = \int_{z_i}^{z_f} p(z)dz \tag{5}$$

where z_i and z_f are the initial and final distance of the wall from the midplane. The work per unit area thus calculated was used to obtain γ using eq 2.

2.3.5. Corrugated Cleaving Walls. To measure the interfacial free energy of the (110) plane in a hard cube crystal, we needed to implement corrugated walls[37] compatible with the zigzagging interface; otherwise, the crystal would spontaneously reorient during the cleaving and merging processes. Here, we present a simplified implementation for corrugated walls that only interact with the centroids of the particles.

Let the plane be corrugated along the y-axis. The corrugated wall was simulated through a triangular wave given by the following function for the z-coordinate of the wall (z_{wall}) at a given y-coordinate and position of the wall z:

$$z_{\mathrm{wall},\pm}(y, z) = \left| y \bmod \lambda - \frac{\lambda}{2} \right| - \frac{\lambda}{4} \mp \frac{\lambda}{4} + z \tag{6}$$

https://doi.org/10.1021/acs.jpcb.1c01737
J. Phys. Chem. B 2021, 125, 5160−5170

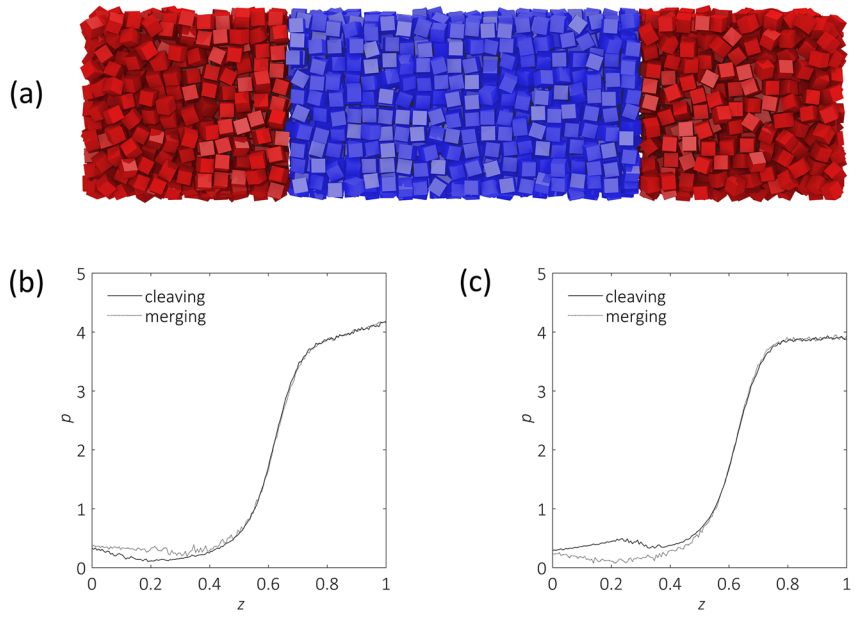

Figure 2. Cleaving walls for hard cubes (100) plane at coexistence pressure $p = 4.0$. (a) Sample configuration at the end of step III. Ordered and disordered phase particles are colored blue and red, respectively. Intermediate configurations at other steps are shown in the Supporting Information. (b, c) Pressure variation with the position of the cleaving walls with respect to the midplane (quantifying the gap width) for (b) ordered and (c) disordered phase. Step I (cleaving) is shown with a solid line, and step II (merging) is shown with gray line. Scaling for the axes is described in Section 2.2.

where $\pm$ refers to different walls based on the direction of movement during step I, and λ is the wavelength of corrugation along the y-axis. Note that the position of the wall z is defined as the z-coordinate of the leading peaks of the triangular wave facing the direction of movement during step I. In this way, at $z = 0$ neither wall interacts with any particle at the beginning of the simulation.

The final positions of the walls at the end of step I were kept conservatively at $z_{\text{final},\pm} = \pm\left(a_c + \frac{\lambda}{2}\right)$ to ensure that particles cannot interact across the gap. The pressure calculations for the corrugated wall are identical to those for the flat wall. The wavelength λ is determined by the initial conditions of the crystal simulation box and was chosen such that the box length along the y-axis is $L_y = n_p\lambda$, where n_p is the number of particle layers along the y-axis. This choice ensures compatibility with the periodic boundary conditions and cleaves the systems in a manner conforming with the crystal plane. In principle, this approach can be generalized to other topographies with an appropriate wall function.

2.4. Interfacial Potential of Mean Force (PMF). We calculated the PMF experienced by a free particle interacting with a perfect interface of particles in a crystalline arrangement. *NVT* simulations were conducted comprising a single immobile layer of crystalline particles and a free particle. The spacing of the crystalline particles was chosen to be consistent with the volume fraction of the coexistence conditions. Statistics for free particle position were obtained through 10^7 MC cycles. The coordinates of the free particles were histogrammed with a resolution of $0.05a_c$. The PMF experienced at a given bin i is given by

$$\text{PMF}_i = -k_B T \ln\left(\frac{f_i}{f_\infty}\right) \tag{7}$$

where f_i and f_∞ are the visiting frequencies for the ith bin and a distant bin where the particle is not interacting with the immobile particles, respectively. The statistics were sufficient to obtain states with PMF $\sim 7\ k_B T$. For comparison across different systems, the "effective" position of the interface was chosen to correspond to the point where PMF $= 5\ k_B T$.

2.5. Measurement of Interfacial Thickness. We estimate the thickness of the interface using the final configuration at the end of step III of the cleaving process. The interface thickness δ is defined in a manner analogous to phase field models:[39]

$$\phi(z) = \frac{1}{2}\left(1 + \tanh\frac{z}{2\delta}\right) \tag{8}$$

where ϕ is a scalar order parameter and z is the position with respect the interface. For our analysis we define ϕ as

$$\phi = \frac{\rho_s - \rho(z)}{\rho_s - \rho_l} \tag{9}$$

where ρ_s, ρ_l, and $\rho(z)$ are the densities of the bulk solid, bulk liquid, and system at position z. Thus, $\phi = 0$ for the bulk solid, and $\phi = 1$ for the bulk liquid. The starting interfacial configurations are simulated further for 10^6 MC cycles in an *NVT* ensemble to obtain statistics for $\phi(z)$. Equation 8 is fitted to the z vs $\phi(z)$ data using a least-squares method to obtain δ, which is reported in circumradius units (a_c).

3. RESULTS AND DISCUSSION

3.1. Interfacial Free Energy. The calculation was carefully performed to ensure that the process does not significantly alter the bulk behavior of either phase (e.g., by ordering of the disordered phase or disordering of the ordered phase). The process was conducted for various system lengths, and it was observed that the cleaving process influences the structure of a layer ~3 particles deep into the bulk phases. Hence, a system

https://doi.org/10.1021/acs.jpcb.1c01737
J. Phys. Chem. B 2021, 125, 5160−5170

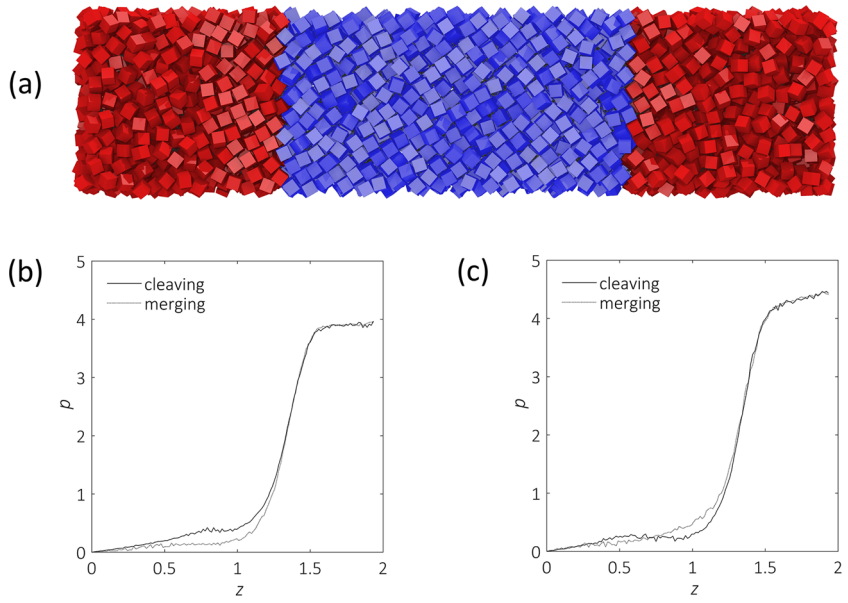

Figure 3. Cleaving walls for hard cubes (110) plane at coexistence pressure $p = 4.0$. (a) Sample configuration at the end of step III. Ordered and disordered phase particles are colored blue and red, respectively. Intermediate configurations at other steps are shown in the Supporting Information. (b, c) Pressure variation with the position of the cleaving walls defined by the leading peak of the corrugated wall (see Section 2.3.5) with respect to the midplane (quantifying the gap width) for (b) ordered and (c) disordered phases. Step I (cleaving) is shown with a solid line, and step II (merging) is shown with a dotted line. Scaling for the axes is described in Section 2.2.

size of $N = 2000$ particles (~20 layers) on each phase was chosen. A sample configuration at the end of step III for the case in which the interfacial plane faces the (100) crystal plane is shown in Figure 2a. Intermediate configurations at other steps are shown in the Supporting Information. The pressure profiles for cleaving and merging cubes at coexistence pressure $p_{co} = 4.0$ are shown in Figure 2b,c for the ordered and disordered phase, respectively.

The interfacial free energy for the (100) orientation of the ordered phase was determined as $\gamma_{100} = 0.042 \pm 0.007$. Attempts to calculate the interfacial tension for the (110) orientation γ_{110} with a flat (i.e., noncorrugated) cleaving wall resulted in the ordered phase reorienting in the (100) direction upon merging. This rapid reorienting is rather unique to cubes as we have tested a variety of orientations of other polyhedral crystals without facing the same problem. There could be several reasons for this. The tendency to reorientation indicates that $\gamma_{100} < \gamma_{110}$, so that the system relaxes toward the more stable interface. The short time scale of this process is likely facilitated by the unusually high diffusivity[13] and vacancy concentration[32,33] in the ordered phase for cubes. Fast crystal domain reorientation is consistent with our observations in a previous study[24] that hard cubes exhibit fast grain resolution dynamics. Also, because the disordered phase is cleaved by a flat wall, the cubes in the closest layers tend to align parallel to it, which in turn tend to realign (flatten) the closest zigzag (110) layer of the ordered phase during the merging step. This limitation was resolved with implementation of a corrugated cleaving wall[37] as described in Section 2.3.5. This approach allows for the disordered phase to be cleaved with a zigzag presentation of the particles compatible with the (110) crystal plane. The final configuration with (110) interfaces at the end of step III and pressure profiles for both phases are shown in Figure 3.

The interfacial free energy for the (110) orientation of the ordered phase was determined as $\gamma_{110} = 0.090 \pm 0.010$. This value is more than twice γ_{100}, confirming that this difference is the main force driving the crystal reorientation with a flat wall observed earlier. The physical reason for why $\gamma_{100} < \gamma_{110}$ can be rationalized by examining the entropic and enthalpic effects associated with the particles in the disordered region in contact with the different ordered planes, to be referred to here as the *wetting layer*. The pV component of the enthalpy (and free energy) favors smaller volumes or denser packing (due to closer contact) of the wetting layer; likewise, a more efficient packing (attained by partial lateral alignment) would favor packing entropy of that layer. As the potential of mean force (PMF) calculations reveal (Figure 4), the (110) plane produces a longer-range repulsive field, which is a consequence of its rougher and more intrusive profile (Figure 4, inset). This also translates into a thicker wetting layer as shown in Figure 5. These observations are consistent with a larger free energy

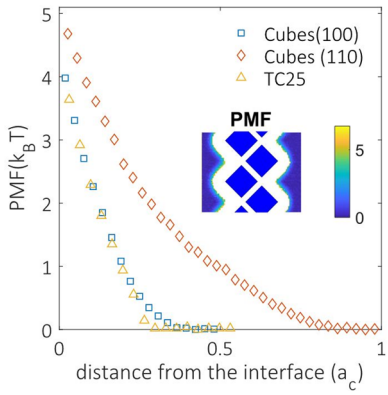

Figure 4. Interfacial potentials of mean force (PMF) at coexistence for various cases. Inset shows two-dimensional PMF surface for the (110) plane of hard cubes, where crystalline cubes (blue) are placed in the middle at their fixed positions in the calculation. Details on the calculation are provided in Section 2.4.

https://doi.org/10.1021/acs.jpcb.1c01737
J. Phys. Chem. B 2021, 125, 5160−5170

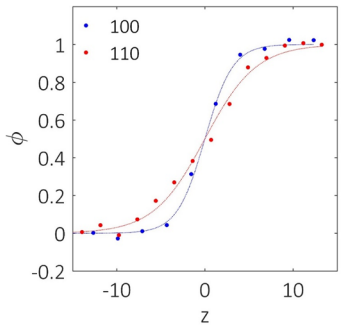

Figure 5. Scalar order parameter ϕ as a function of position with respect to the interface (z, in circumradius a_C units) for two crystal planes of hard cubes. The interfacial thicknesses of (100) and (110) crystal planes were found to be $\delta_{100} = 1.6 \pm 0.2$ and $\delta_{100} = 2.9 \pm 0.3$, respectively. Details on the calculation are provided in Section 2.5.

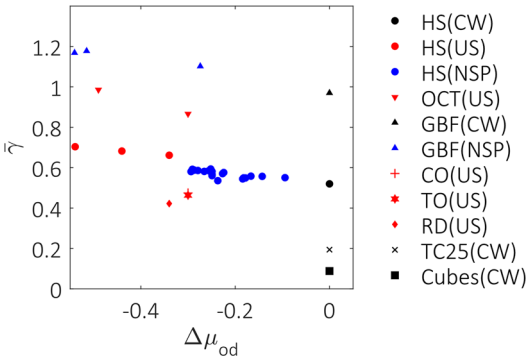

Figure 6. Reduced interfacial free energy $\overline{\gamma}$ at a given supersaturation $\Delta\mu_{od}$ for various shapes (HS, hard spheres; OCT, octahedra; GBF, gyrobifastigia; CO, cuboctahedra; TO, truncated octahedra; RD, rhombic dodecahedra; TC25, truncated cubes with $s = 0.25$, and cubes) reported in the literature using a variety of methods (CW, cleaving walls; US, umbrella sampling and classical nucleation theory; NSP, nucleus-size pinning with classical nucleation theory). Data sources: HS(CW);[37] HS(US);[19] HS(NSP);[23] OCT(US);[22] GBF-(CW);[46] GBF(NSP);[23] CO-TO-RD(US);[21] cubes and TC25, this work.

penalty in the 110 wetting layer, and hence, $\gamma_{110} > \gamma_{100}$. Based on these physical considerations, we further anticipate that $\gamma_{111} > \gamma_{110} > \gamma_{100}$.

On the basis of the γ values thus calculated, a Wulff construction[40−43] could be performed to obtain information about the nucleus geometry. The governing principle of Wulff construction states that the length h of a perpendicular to a crystal plane passing through the centroid is proportional to its interfacial free energy γ. On the basis of this principle, the perpendiculars of (100) and (110) facets should be related as $h_{110} = 2.14h_{100}$. This relation would put the (110) plane outside the inner volume enclosed by the (100) plane since $h_{110} > \sqrt{2}h_{100}$. This implies that if we restrict ourselves to the close-packed facets,[43] the (110) should not show up in an equilibrium nucleus geometry. Regardless, since the (100) facet is the most close-packed[43] facet for this crystal, γ_{100} can be used as a representative value for comparison across different shapes.

We use reduced interfacial free energies $\overline{\gamma}$ as defined in Section 2.2 for comparison across different shapes. In most studies of hard polyhedra, the interfacial free energy has been calculated indirectly through nucleation free energy barrier calculations[18,21] leveraging classical nucleation theory (CNT). These approaches are sensitive to the definition of the order parameter used to ascertain the interface of the nucleus.[44] Nevertheless, these indirect estimates for hard spheres are very much comparable to those obtained from direct methods including the cleaving-walls approach.[45] Hence, we use CNT estimates for comparison among shapes when results from any direct method are unavailable.

At coexistence, the value of the reduced interfacial free energy for the (100) crystal facet in cubes ($\overline{\gamma}_{100} = 0.088$) is about one-sixth the value for hard spheres ($\overline{\gamma}_{HS} \sim 0.52$ for all closed packed orientations). For comparison, orientationally average interfacial free energies reported for polyhedral particles (at the disorder−order phase transition) have been at most 20% lower than that of hard spheres (e.g., for cuboctahedra, truncated octahedra, and rhombic dodecahedra),[21] and often higher than that (e.g., for octahedra and gyrobifastigia).[22,23] We illustrate these observations in Figure 6 where we plot reduced interfacial free energy $\overline{\gamma}$ at a given supersaturation $\Delta\mu_{od}$ for a number of shapes as reported in the literature. It is evident that cubes have by far the lowest value of reduced interfacial free energy, which generally increases with $\Delta\mu_{od}$.

Physically, the small $\overline{\gamma}$ for hard cubes implies a small penalty for creating solid−liquid interfaces, which correlates with the observation of a relatively high incidence of ordered and disordered domains coexisting next to each other in both the disordered and ordered phases. This results in a significant concentration of ordered domains in the disordered phase and hence a high fraction of ordered particles (about 3% at coexistence compared to less than 0.05% for hard spheres). Likewise, the high content (>6%) of mobile vacancies in the solid phase[32] connotes some localized liquid-like behavior. This similarity between some local configurations from its disordered and ordered phases means that both phases share a fraction of the same phase space in the terms of translational and orientational order, which enhances their interfacial affinity.

The low γ could also be indicative of the proximity between the binodal and spinodal conditions for cubes, as a zero interfacial tension is a characteristic of the spinodal point in other systems.[47,48] This hypothesis is strengthened by the fact that the orientational correlation length diverges with pressure (see SI). We attempted a calculation of γ for cubes at finite degrees of supersaturation, but the results were inconclusive due to large statistical variations associated with a significant tendency for ordering in the disordered phase. A more complete picture of the consequences of low $\overline{\gamma}$ values is provided in the next section through a theoretical analysis.

We also examined the effect of a small perturbation to the cubic shape on interfacial tension by computing $\overline{\gamma}_{100}$ for truncated cubes with truncation parameter[16] $s = 0.25$, hereafter referred to as TC25. The phase behavior is similar to that of hard cubes, with a first-order transition from a disordered phase to a simple cubic crystal. Moreover, the disordered phase also has an abundance of cubatic fluctuations, and the ordering transition progresses spontaneously at very low supersaturations. We also calculated the free energy barrier for the TC25 disorder-to-order transition at coexistence through umbrella sampling as described elsewhere[24] (see crucial details in the Supporting Information). The free energy profile as a function of the fraction of ordered particles ($x_{ordered}$) at coexistence pressure for TC25 is shown in Figure 7, along with the

https://doi.org/10.1021/acs.jpcb.1c01737
J. Phys. Chem. B 2021, 125, 5160−5170

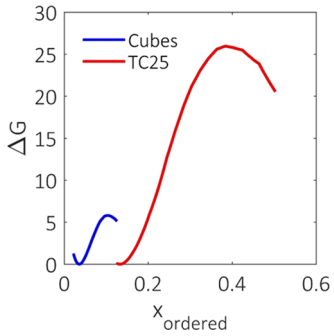

Figure 7. Free energy (ΔG) profile calculated as a function of fraction of ordered particles ($x_{ordered}$) for TC25 via umbrella sampling at coexistence p = 3.64. Previously reported[24] free energy profile for a hard cubes system of identical size (N = 1000) is also shown for comparison. Free energy is in k_BT units.

previously reported[24] results for hard cubes. At coexistence, the free energy barrier for TC25 is over three times larger than that of hard cubes. While there is no clear theoretical framework that can describe the exact relationship between $\overline{\gamma}$ and ΔG^* for this nonclassical phase transition, the much higher barrier would indicate a correspondingly higher value for interfacial free energy. Indeed, we find that the interfacial free energy for the (100) plane of TC25 using the cleaving-walls method at the coexistence pressure[14] p_{co} = 3.64 is $\overline{\gamma}_{100,TC25}$ = 0.194, which is about 2 times that for hard cubes. Another important observation is that $x_{ordered}$ at both the disordered-state basin and the top of the barrier is much higher for TC25 compared to cubes. We note, however, that the order parameter definitions (see Supporting Information) are not identical for hard cubes and TC25, and hence, the $x_{ordered}$ for the two systems cannot be unambiguously compared. While the PMF for cubes and TC25 (associated with the 100 plane) are expectedly comparable, the densities of the coexistence phases are higher for TC25 than those for cubes, which would be expected to increase γ.

An interesting trend in Figure 6 is that particles' shapes having a greater similarity to cubes tend to have a lower γ (e.g., TC25 and CO). This could reflect the fact that a preference of local ordered motifs with 6-fold coordination and smaller unit cells is easier to generate than structures requiring the coordination for more nearest-neighbor particles (like 8 or 12) and larger unit cells. The low coordination number of cube-like shapes is a likely contributor to low γ values by promoting low-free-energy-cost 6-fold configurations in a route to the ordered phases they form (even if not a simple cubic). Since no other hard particle is able to order with a smaller coordination number and unit cell, we surmise that hard cubes likely possess the lowest γ value of all athermal systems at the order−disorder transition (note that we exclude the case of tetrahedra whose isotropic phase does not transition into a simple-unit-cell solid[49]).

3.2. Theoretical Quantification of Cubatic Fluctuations. We aim to provide a simple description of how the fraction of ordered particles ($x_{ordered}$) compounding the local solid-like fluctuations in the disordered phase is related to $\overline{\gamma}$ at a given supersaturation $\Delta\mu_{od}$. In this model, the cubatic fluctuations are in the form of nuclei which are noninteracting with each other and are distributed uniformly throughout the bulk.[50] With $\Delta G(n)$ as the free energy change associated with the formation of an ordered cluster of size n (analogous to n particles), classical nucleation theory (CNT) provides the following expression:

$$\Delta G(n) = \Delta\mu_{od} n + A\overline{\gamma} n^{2/3} \tag{10}$$

where A is a geometric factor capturing the shape of the nucleus assuming that its surface area scales with the two-thirds power of the volume. For simplicity, we assume that both the inner and the interfacial regions of a cluster can be described by μ_o and $\overline{\gamma}$. This is not true for clusters smaller than a characteristic length, and there are models that could be used to account for such an effect.[51−53] As such, our model will overestimate $x_{ordered}$ if $\overline{\gamma}$ is higher for smaller clusters than larger ones in the system being considered, as has been found to be the case in hard spheres.[54]

For steady state conditions for a system evolving from the metastable disorder-phase basin, the distribution of fraction of particles x_n belonging to clusters of size n can be described by the law of mass action[55] as

$$x_n = n x_0^n e^{-\Delta G(n)} \tag{11}$$

where x_0 is the fraction of disordered particles. We note that such a formulation assumes no intercluster interactions; that is, the effect of impingements between clusters is neglected so that each cluster is independent from others and only surrounded by disordered cubes. Further, the ordered clusters exhibiting a range of representative sizes are assumed to be well-mixed (uniformly distributed) throughout a "continuous" phase of disordered cubes. Despite the limitations imposed by these assumptions (i.e., a scenario of relatively dilute clusters), this model forms a good basis for illustrating the consequences of interfacial tension on the concentration of ordered particles in the metastable disordered basin. We define the metastable basin as a disordered phase that may contain clusters up to the critical cluster size at the top of the barrier defined as

$$n^* = \left(\frac{2A\overline{\gamma}}{3|\Delta\mu_{od}|}\right)^3 \tag{12}$$

The fraction of ordered particles in the basin can then be evaluated as an integral over various sizes of ordered clusters described by eq 11:

$$x_{ordered} = \int_{0^+}^{n^*} x_n \, dn \tag{13}$$

A discrete version of the model could also be formulated considering only integer nucleus sizes (see Supporting Information). We favor here the continuous version of the model as it avoids discontinuous jumps in values and makes trends easier to follow. With applying mass balance on all particles

$$x_0 + x_{ordered} = 1 \tag{14}$$

Since the left-hand side of eq 14 (when coupled to eqs 12 and 13) consists of continuous functions and takes a value of zero for x_0 = 0 and a value greater than unity for x_0 = 1, then the intermediate value theorem ensures that a solution for $x_0 \in [0, 1]$ exists where the equality of eq 14 holds. We can then numerically solve for this value of x_0 at any given conditions of $\Delta\mu_{od}$ and $\overline{\gamma}$.

We can follow the consequences of this mass action-derived classical nucleation theory (MADCNT) model in the context of the cubatic fluctuations observed in the disordered phase of

https://doi.org/10.1021/acs.jpcb.1c01737
J. Phys. Chem. B 2021, 125, 5160−5170

hard cubes by evaluating $x_{ordered}$ as a function of $\Delta\mu_{od}$ and $\overline{\gamma}$ for a particular case. For simplicity, if the ordered clusters are spherical, the geometric factor will be

$$A = (36\pi)^{1/3} \tag{15}$$

As an example, Figure 8a shows a plot of $x_{ordered}$ as a function of $\Delta\mu_{od}$ and $\overline{\gamma}$.

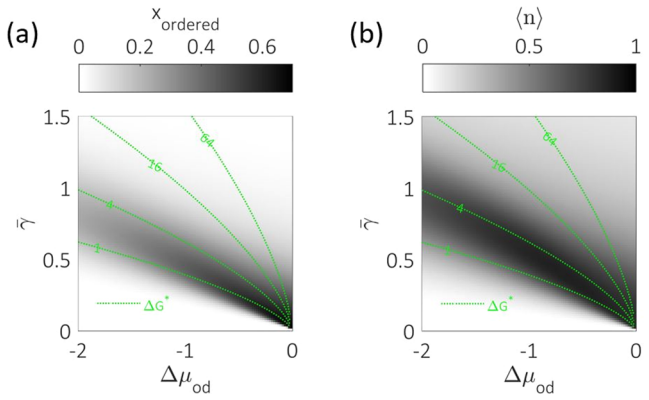

Figure 8. Predictions from the MADCNT model for spherical ordered clusters. (a) Fraction of ordered particles $x_{ordered}$ and (b) average cluster size $\langle n \rangle$ as a function of $\Delta\mu_{od}$ and $\overline{\gamma}$. The isolines for the nucleation barrier ΔG^* are shown in green. The calculations were performed with a resolution of 100 points along each axis.

In general, $x_{ordered}$ remains relatively low (<0.01) except for a diagonal "band" where it can get as high as 0.697. The model also allows us to extract information about the cluster size distribution. Sample distributions of x_n at coexistence as a function of cluster size n are shown in Figure 9. Ordered

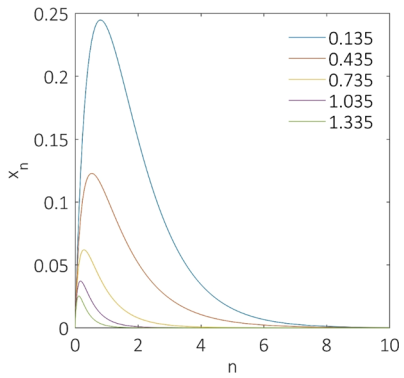

Figure 9. Sample distributions (x_n) of ordered particles over various cluster sizes (n) at coexistence for various values of $\overline{\gamma}$ (given in legend) as predicted by the MADCNT model.

clusters predominantly exist in clusters of small sizes, with the spread of cluster sizes generally decreasing with increasing $\overline{\gamma}$. It is informative to evaluate the average cluster size:

$$\langle n \rangle = \frac{x_{ordered}}{\int_{0^+}^{n^*} x_0^n e^{-\Delta G(n)} dn} \tag{16}$$

Figure 8b reveals that the average cluster size generally correlates with $x_{ordered}$, also attaining higher values along the diagonal band.

The trends in these MADCNT predictions can be understood by considering two effects at play relating to the metastable basin: its depth (embodied by $\Delta G(n^*)$) and its width (embodied by n^*). The width of the basin, n^*, determines the upper limit to the integral in eq 13. A larger n^* would imply that more numerous ordered species are competing against the disordered particles, resulting in a larger $x_{ordered}$. Hence, the width contributes positively to $x_{ordered}$. On the other hand, the depth of the basin is related to the nucleation barrier:

$$\Delta G(n^*) = \Delta G^* = \frac{4(A\overline{\gamma})^3}{27|\Delta\mu_{od}|^2} \tag{17}$$

Also, since $\Delta G(n) < \Delta G(n^*)$, larger values will translate into smaller exponential factors within the integral in eq 13, making the larger clusters rare. Hence, an increased depth of the metastable basin contributes negatively to $x_{ordered}$. Since both width and depth of the metastable basin increase with $\overline{\gamma}$ and decrease with $\Delta\mu_{od}$, the following three distinct regions in the plots of Figure 8 can be identified depending on whether one effect dominates or both effects are in play:

I. Bottom-left triangular region: This region has very low $x_{ordered} \ll 1$ due to narrow metastable basins ensuing from a low $\overline{\gamma}$ and high $|\Delta\mu_{od}|$. In practice, it would be very difficult to sustain a metastable state located in this region due to the very small critical nucleus sizes and barriers (see isolines in Figure 8), which will likely manifest as a spinodal decomposition. Interestingly, the line for $n^* = 1$ demarcates the boundary of this region where $n^* < 1$.

II. Top-right triangular region: This region also has a low $x_{ordered} \ll 1$ but due to reasons different from those for region I. Due to the high $\overline{\gamma}$, the basins are wide and deep. This would result in a rather robust metastable state with the rare occurrence of nuclei, consistent with systems where nucleation and growth is the mechanism of phase transition. Generally, $x_{ordered}$ decreases as $\overline{\gamma}$ increases (interfaces become more expensive) and/or as $\Delta\mu_{od}$ approaches zero (ordered phase becomes relatively less stable). In contrast with region I, $\langle n \rangle$ is slightly higher because larger clusters are being considered. In this region, we can sufficiently describe the fraction of ordered particles through MADCNT, since a low fraction implies the nuclei are unlikely to interact with each other. The values of $x_{ordered}$ predicted by the model in this scenario have been validated for specific conditions for hard spheres and are consistent with predictions of models that use appropriate corrections for interfacial tension as a function of nucleus size.[54]

III. Downward diagonal band: In this region, neither of the effects dominate, leading to a metastable basin that is neither too narrow nor too deep. This results in a non-negligible $x_{ordered}$ that could take up values greater than 0.5, especially near the lower-right corner (low $\overline{\gamma}$, $|\Delta\mu_{od}|$). This is a scenario that MADCNT is ill-suited to describe since beyond a certain $x_{ordered}$ the ordered clusters are likely to interact with each other and form motifs that are not described by eq 10. Indeed, at sufficiently high $x_{ordered}$, a percolating network of ordered clusters might form. We refrain from assigning a percolation threshold as it will depend on the cluster size distribution which varies with conditions $\overline{\gamma}$, $|\Delta\mu_{od}|$. For example, for completely uncorrelated ordered particles distributed throughout the bulk, the three-

https://doi.org/10.1021/acs.jpcb.1c01737
J. Phys. Chem. B 2021, 125, 5160−5170

dimensional percolation threshold for site percolation of the intrinsic crystal lattice might be an appropriate bound. The band becomes more diffused as we go to higher supersaturations, eventually connecting regions I and II.

While $\overline{\gamma}$ and $\Delta\mu_{od}$ are easy-to-interpret physical properties, the trends get simplified when we evaluate $x_{ordered}$ as a function of ΔG^* and n^*, surrogates of depth and width of the metastable basin, respectively, as shown in Figure 10. We

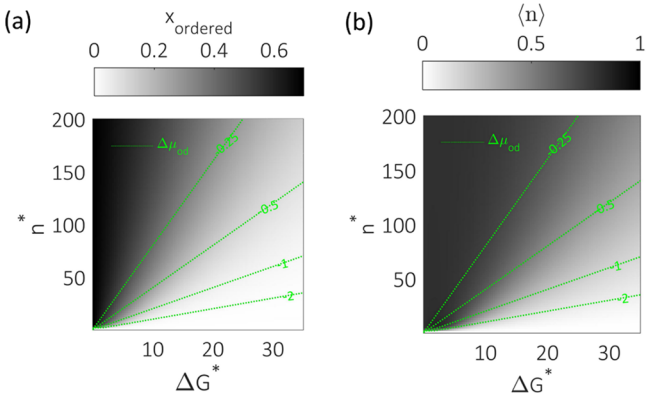

Figure 10. Predictions from the MADCNT model for spherical ordered clusters with (a) fraction of ordered particles $x_{ordered}$ and (b) average cluster size $\langle n \rangle$ as a function of n^* and ΔG^*. The isolines for the supersaturation $\Delta\mu_{od}$ are shown in green. The calculations were performed with a resolution of 100 points along each axis.

notice that regions I and II are mapped into a single triangular region (light area in Figure 10), and $x_{ordered}$ generally increases with increasing n^* and/or decreasing ΔG^*. Thus, the fraction of ordered particles in the metastable phase increases with shallower and wider basins. We note that this alternative mapping preserves the general trends described earlier, but it shrinks certain areas of Figure 8 and expands others, with certain regions involving infeasible/unusual conditions.

It is instructive to compare Figure 8a with Figure 6. While a direct quantitative comparison may be difficult since the geometric factor A is system specific, it can be observed that most shapes would likely be placed in region II given the relatively low concentration of ordered particles observed in the metastable disordered phases of those systems. On the other hand, both cubes and TC25 could be placed in region III by the virtue of their low $\overline{\gamma}$, which is corroborated by the observation of non-negligible $x_{ordered}$ in their metastable phases in simulations and can be associated with a wide, shallow metastable basin.

The validity of a nucleation scenario rests on the basic assumption that at the early stages of phase transformation the nuclei of the incipient phase are rare and grow without interacting with other nuclei before approaching their critical size. This would largely hold for region II but would eventually not be true for systems in region III. For cubes, an abundance of cubatic fluctuations of the incipient ordered phase (as predicted for lower interfacial free energy) would violate this assumption. Under such circumstances, the dominant mechanism cannot be nuclei growth by conversion of disordered particles at the interface since there would also exist interfaces between ordered domains of non-negligible size. Usually, such an impingement of nuclei leads to a halt in growth[56] and the formation of a final polycrystalline state. However, as illustrated in our previous publication,[24] hard cubes exhibit fast dynamics of grain resolution by quickly reorienting intermediate layers along the boundary of two grains and then propagating a uniform alignment. Hence, any two impinging clusters could merge in a process similar to Oswald ripening. An increase in concentration of ordered clusters would increase instances of such growth mechanisms. There would be a critical concentration beyond which such instances of consolidation (or ripening) would become more probable than the breaking of clusters into smaller clusters. This would be consistent with our observation in a previous report[24] of a critical concentration of ordered cubes being required to effect the disorder-to-order phase transition. Indeed, we found that cubes exhibit a transition that involves ordered phase nuclei gradually consolidating by resolving grain boundaries through local reorientation events.

4. CONCLUSION AND OUTLOOK

In this study, we implemented the cleaving-walls method to directly measure order−disorder interfacial free energy for the (100) and (110) crystal planes of hard cubes. We found them to be substantially lower than those for other reported cases of hard-core particles where nucleation and growth are reported. Our MADCNT model predicts that a lower interfacial tension gives rise to more abundant ordered clusters in the disordered phase, which could explain the abundance of cubatic fluctuations in the disordered phase for hard cubes. We also find that hard truncated cubes (TC25) have a higher $\overline{\gamma}_{100}$ than hard cubes which also translates into higher free energy barriers at comparable coexistence conditions.

There are, however, several open questions regarding the nonclassical characteristics of the ordering phase transition of hard cubes. It would be of interest to attain a deeper understanding of why hard cubes have a lower surface tension than other shapes. Given that TC25 also has a smaller $\overline{\gamma}$ compared to other particle shapes points to the cubic lattice structure of the ordered phase, and its known peculiarities, as playing a central role. Of course, cubic symmetry may not be a sufficient condition for a low $\overline{\gamma}$; indeed, we expect that if interparticle attractions are enacted among cubes, $\overline{\gamma}$ could be made significatively larger. In this context, interfacial tension calculations for other hard-core shapes and crystal planes would be informative and could help illuminate any trends therein. For example, while we found that truncation of the cubes increases the interfacial free energy (i.e., going from perfect cubes to TC25), it would be worthwhile to explore if larger perturbations can alter the behavior to the point where the classical nucleation and growth picture becomes a valid description. In assessing the role of γ in the ordering of cubes and concomitant theories, it is also important to keep in mind that since most cubatic fluctuations are small and encompass only 10 or fewer particles, bulk-like domains and their interfaces are not well-defined. Further, as we have noticed in our simulations, the effect of the interface could reach ∼3 particles deep into either phase. There are interesting approaches to address these effects[53,54,57,58] and describe the free energy of small clusters. Even in cases where nuclei are large enough to have well-defined geometries, it would be interesting to investigate the morphology of the nuclei through Wulff construction,[40,43] especially in cases with aspherical nuclei,[23] as this would help evaluating the geometric factor (A) in CNT-like theories.

https://doi.org/10.1021/acs.jpcb.1c01737
J. Phys. Chem. B 2021, 125, 5160−5170

Further studies could aim to provide a more rigorous theoretical treatment that is applicable to region III described in Section 3.2. The key element would be a description of ordered motifs that are preferred when the classical theory predicts the presence of too many ordered nuclei. At high $\overline{\gamma}$, there would be a preference to make compact motifs like nuclei, but at lower $\overline{\gamma}$ the ordered domains could comprise loose dendritic structures. Also needing a description is a mechanism that captures how the ordered motifs grow, analogous to nucleus growth in CNT. For noncompact ordered domains, the interfacial contribution to the free energy would not necessarily grow monotonously with the concentration of ordered particles (see SI), hence leading to more complex free energy landscapes.

■ ASSOCIATED CONTENT

Supporting Information

The Supporting Information is available free of charge at https://pubs.acs.org/doi/10.1021/acs.jpcb.1c01737.

Additional details pertaining to the cleaving-walls method, the truncated cube system, and the MADCNT model (PDF)

■ AUTHOR INFORMATION

Corresponding Author

Fernando A. Escobedo − *R. F. Smith School of Chemical and Biomolecular Engineering, Cornell University, Ithaca, New York 14853, United States;* orcid.org/0000-0002-4722-9836; Email: fe13@cornell.edu

Author

Abhishek K. Sharma − *R. F. Smith School of Chemical and Biomolecular Engineering, Cornell University, Ithaca, New York 14853, United States*

Complete contact information is available at: https://pubs.acs.org/10.1021/acs.jpcb.1c01737

Notes

The authors declare no competing financial interest.

■ ACKNOWLEDGMENTS

Funding support from NSF award CBET-1907369 is gratefully acknowledged. We would also like to acknowledge Dr. Vikram Thapar for sharing base simulation code, Dr. Karthik Nayani for sharing useful literature, and Prof. Donald Koch and Prof. Marjolein Dijkstra for insightful discussions.

■ REFERENCES

(1) Henzie, J.; Grünwald, M.; Widmer-Cooper, A.; Geissler, P. L.; Yang, P. Self-Assembly of Uniform Polyhedral Silver Nanocrystals into Densest Packings and Exotic Superlattices. *Nat. Mater.* **2012**, *11*, 131−137.

(2) Seo, D.; Park, J. C.; Song, H. Polyhedral Gold Nanocrystals with Oh Symmetry: From Octahedra to Cubes. *J. Am. Chem. Soc.* **2006**, *128*, 14863−14870.

(3) Tao, A. R.; Habas, S.; Yang, P. Shape Control of Colloidal Metal Nanocrystals. *Small* **2008**, *4*, 310−325.

(4) Cademartiri, L.; Bishop, K. J. M. Programmable Self-Assembly. *Nat. Mater.* **2015**, *14*, 2−9.

(5) Whitesides, G. M.; Boncheva, M. Beyond Molecules: Self-Assembly of Mesoscopic and Macroscopic Components. *Proc. Natl. Acad. Sci. U. S. A.* **2002**, *99*, 4769−4774.

(6) Whitesides, G. M.; Grzybowski, B. Self-Assembly at All Scales. *Science* **2002**, *295*, 2418−2421.

(7) Cademartiri, L.; Bishop, K. J. M.; Snyder, P. W.; Ozin, G. A. Using Shape for Self-Assembly. *Philos. Trans. R. Soc., A* **2012**, *370*, 2824−2847.

(8) Manoharan, V. N. Colloidal Matter: Packing, Geometry, and Entropy. *Science* **2015**, *349*, 1253751.

(9) Kempa, T. J.; Kim, S. K.; Day, R. W.; Park, H. G.; Nocera, D. G.; Lieber, C. M. Facet-Selective Growth on Nanowires Yields Multi-Component Nanostructures and Photonic Devices. *J. Am. Chem. Soc.* **2013**, *135*, 18354−18357.

(10) Bian, K.; Schunk, H.; Ye, D.; Hwang, A.; Luk, T. S.; Li, R.; Wang, Z.; Fan, H. Formation of Self-Assembled Gold Nanoparticle Supercrystals with Facet-Dependent Surface Plasmonic Coupling. *Nat. Commun.* **2018**, *9*, 2365.

(11) Pietrobon, B.; McEachran, M.; Kitaev, V. Synthesis of Size-Controlled Faceted Pentagonal Silver Nanorods with Tunable Plasmonic Properties and Self-Assembly of These Nanorods. *ACS Nano* **2009**, *3*, 21−26.

(12) Damasceno, P. F.; Engel, M.; Glotzer, S. C. Predictive Self-Assembly of Polyhedra into Complex Structures. *Science (Washington, DC, U. S.)* **2012**, *337*, 453−457.

(13) Agarwal, U.; Escobedo, F. A. Mesophase Behaviour of Polyhedral Particles. *Nat. Mater.* **2011**, *10*, 230−235.

(14) Gantapara, A. P.; De Graaf, J.; Van Roij, R.; Dijkstra, M. Phase Behavior of a Family of Truncated Hard Cubes. *J. Chem. Phys.* **2015**, *142*, 054904.

(15) Ni, R.; Gantapara, A. P.; De Graaf, J.; Van Roij, R.; Dijkstra, M. Phase Diagram of Colloidal Hard Superballs: From Cubes via Spheres to Octahedra. *Soft Matter* **2012**, *8*, 8826−8834.

(16) Gantapara, A. P.; De Graaf, J.; Van Roij, R.; Dijkstra, M. Phase Diagram and Structural Diversity of a Family of Truncated Cubes: Degenerate Close-Packed Structures and Vacancy-Rich States. *Phys. Rev. Lett.* **2013**, *111*, 015501.

(17) Onsager, L. The Effects of Shape on the Interaction of Colloidal Particles. *Ann. N. Y. Acad. Sci.* **1949**, *51*, 627−659.

(18) Auer, S.; Frenkel, D. Prediction of Absolute Crystal-Nucleation Rate in Hard-Sphere Colloids. *Nature* **2001**, *409*, 1020−1023.

(19) Auer, S.; Frenkel, D. Numerical Prediction of Absolute Crystallization Rates in Hard-Sphere Colloids. *J. Chem. Phys.* **2004**, *120*, 3015−3029.

(20) Filion, L.; Hermes, M.; Ni, R.; Dijkstra, M. Crystal Nucleation of Hard Spheres Using Molecular Dynamics, Umbrella Sampling, and Forward Flux Sampling: A Comparison of Simulation Techniques. *J. Chem. Phys.* **2010**, *133*, 244115.

(21) Thapar, V.; Escobedo, F. A. Localized Orientational Order Chaperones the Nucleation of Rotator Phases in Hard Polyhedral Particles. *Phys. Rev. Lett.* **2014**, *112*, 048301.

(22) Sharma, A. K.; Thapar, V.; Escobedo, F. A. Solid-Phase Nucleation Free-Energy Barriers in Truncated Cubes: Interplay of Localized Orientational Order and Facet Alignment. *Soft Matter* **2018**, *14*, 1996−2005.

(23) Sharma, A. K.; Escobedo, F. A. Nucleus-Size Pinning for Determination of Nucleation Free-Energy Barriers and Nucleus Geometry. *J. Chem. Phys.* **2018**, *148*, 184104.

(24) Sharma, A. K.; Escobedo, F. A. Disorder Foreshadows Order in Colloidal Cubes. *J. Phys. Chem. B* **2018**, *122*, 9264−9273.

(25) Gasser, U.; Weeks, E. R.; Schofield, A.; Pusey, P. N.; Weitz, D. A. Real-Space Imaging of Nucleation and Growth in Colloidal Crystallization. *Science (Washington, DC, U. S.)* **2001**, *292*, 258−262.

(26) Tao, A.; Sinsermsuksakul, P.; Yang, P. Polyhedral Silver Nanocrystals with Distinct Scattering Signatures. *Angew. Chem., Int. Ed.* **2006**, *45*, 4597−4601.

(27) Sun, Y.; Xia, Y. Shape-Controlled Synthesis of Gold and Silver Nanoparticles. *Science (Washington, DC, U. S.)* **2002**, *298*, 2176−2179.

(28) Gong, J.; Newman, R. S.; Engel, M.; Zhao, M.; Bian, F.; Glotzer, S. C.; Tang, Z. Shape-Dependent Ordering of Gold

Nanocrystals into Large-Scale Superlattices. *Nat. Commun.* **2017**, *8*, 14038.
(29) Shukla, N.; Liu, C.; Roy, A. G. Oriented Self-Assembly of Cubic FePt Nanoparticles. *Mater. Lett.* **2006**, *60*, 995−998.
(30) Metropolis, N.; Rosenbluth, A. W.; Rosenbluth, M. N.; Teller, A. H.; Teller, E. Equation of State Calculations by Fast Computing Machines. *J. Chem. Phys.* **1953**, *21*, 1087−1092.
(31) Lee, S.; Teich, E. G.; Engel, M.; Glotzer, S. C. Entropic Colloidal Crystallization Pathways via Fluid-Fluid Transitions and Multidimensional Prenucleation Motifs. *Proc. Natl. Acad. Sci. U. S. A.* **2019**, *116*, 14843−14851.
(32) Smallenburg, F.; Filion, L.; Marechal, M.; Dijkstra, M. Vacancy-Stabilized Crystalline Order in Hard Cubes. *Proc. Natl. Acad. Sci. U. S. A.* **2012**, *109*, 17886−17890.
(33) van der Meer, B.; van Damme, R.; Dijkstra, M.; Smallenburg, F.; Filion, L. Revealing a Vacancy Analog of the Crowdion Interstitial in Simple Cubic Crystals. *Phys. Rev. Lett.* **2018**, *121*, 258001.
(34) James, D.; Beairsto, S.; Hartt, C.; Zavalov, O.; Saika-Voivod, I.; Bowles, R. K.; Poole, P. H. Phase Transitions in Fluctuations and Their Role in Two-Step Nucleation. *J. Chem. Phys.* **2019**, *150*, 074501.
(35) Gottschalk, S.; Lin, M. C.; Manocha, D. OBB Tree: A Hierarchical Structure for Rapid Interference Detection. *Proc. 23rd Annu. Conf. Comput. Graph. Interact. Technol. SIGGRAPH 1996* **1996**, 171−180.
(36) Davidchack, R. L.; Laird, B. B. Direct Calculation of the Hard-Sphere Crystal/Melt Interfacial Free Energy. *Phys. Rev. Lett.* **2000**, *85*, 4751−4754.
(37) Davidchack, R. L. Hard Spheres Revisited: Accurate Calculation of the Solid-Liquid Interfacial Free Energy. *J. Chem. Phys.* **2010**, *133*, 234701.
(38) De Miguel, E.; Jackson, G. The Nature of the Calculation of the Pressure in Molecular Simulations of Continuous Models from Volume Perturbations. *J. Chem. Phys.* **2006**, *125*, 164109.
(39) Boettinger, W. J.; Warren, J. A.; Beckermann, C.; Karma, A. Phase-Field Simulation of Solidification. *Annu. Rev. Mater. Res.* **2002**, *32*, 163−194.
(40) Ogura, T.; Hayami, R.; Kadota, M. Kinetics and Mechanism of Crystallization of Lithium Silicate Glasses. *Yogyo Kyokaishi* **1968**, *76*, 277−284.
(41) Tutton, A. E. H.; Hilton, H. Mathematical Crystallography and the Theory of Groups of Movements. *Math. Gaz.* **1904**, *2*, 387.
(42) Bealing, C. R.; Baumgardner, W. J.; Choi, J. J.; Hanrath, T.; Hennig, R. G. Predicting Nanocrystal Shape through Consideration of Surface-Ligand Interactions. *ACS Nano* **2012**, *6*, 2118−2127.
(43) Frank, F. C. Crystal Growth and Dislocations. *Adv. Phys.* **1952**, *1*, 91−109.
(44) Zimmermann, N. E. R.; Vorselaars, B.; Espinosa, J. R.; Quigley, D.; Smith, W. R.; Sanz, E.; Vega, C.; Peters, B. NaCl Nucleation from Brine in Seeded Simulations: Sources of Uncertainty in Rate Estimates. *J. Chem. Phys.* **2018**, *148*, 222838.
(45) Espinosa, J. R.; Vega, C.; Valeriani, C.; Sanz, E. Seeding Approach to Crystal Nucleation. *J. Chem. Phys.* **2016**, *144*, 034501.
(46) Sharma, A. K.; Escobedo, F. A. Determination of Interfacial Free Energy for Gyrobifastagia. Submitted for publication, 2021.
(47) Fortini, A.; Dijkstra, M.; Schmidt, M.; Wessels, P. P. F. Wall-Fluid and Liquid-Gas Interfaces of Model Colloid-Polymer Mixtures by Simulation and Theory. *Phys. Rev. E - Stat. Nonlinear, Soft Matter Phys.* **2005**, *71*, 051403.
(48) Ni, R.; Belli, S.; Van Roij, R.; Dijkstra, M. Glassy Dynamics, Spinodal Fluctuations, and the Kinetic Limit of Nucleation in Suspensions of Colloidal Hard Rods. *Phys. Rev. Lett.* **2010**, *105*, 7−10.
(49) Haji-Akbari, A.; Engel, M.; Glotzer, S. C. Phase Diagram of Hard Tetrahedra. *J. Chem. Phys.* **2011**, *135*, 194101.
(50) Cheng, B.; Ceriotti, M. Bridging the Gap between Atomistic and Macroscopic Models of Homogeneous Nucleation. *J. Chem. Phys.* **2017**, *146*, 034106.
(51) Wilemski, G. The Kelvin Equation and Self-Consistent Nucleation Theory. *J. Chem. Phys.* **1995**, *103*, 1119−1126.
(52) Ford, I. J. Statistical Mechanics of Nucleation: A Review. *Proc. Inst. Mech. Eng., Part C* **2004**, *218*, 883−899.
(53) Kalikmanov, V. I. Nucleation Theory. *Lect. Notes Phys.* **2013**, *860*, 1−331.
(54) Cacciuto, A.; Auer, S.; Frenkel, D. Solid-Liquid Interfacial Free Energy of Small Colloidal Hard-Sphere Crystals. *J. Chem. Phys.* **2003**, *119*, 7467−7470.
(55) Israelachvili, J. N. Thermodynamic Principles of Self-Assembly. In *Intermolecular and Surface Forces*; Elsevier, 2011; pp 503−534.
(56) Riedel, M. R.; Karato, S. I. Microstructural Development during Nucleation and Growth. *Geophys. J. Int.* **1996**, *125*, 397−414.
(57) Heermann, D. W. Classical Nucleation Theory with a Tolman Correction. *J. Stat. Phys.* **1982**, *29*, 631−640.
(58) Montero De Hijes, P.; Espinosa, J. R.; Bianco, V.; Sanz, E.; Vega, C. Interfacial Free Energy and Tolman Length of Curved Liquid-Solid Interfaces from Equilibrium Studies. *J. Phys. Chem. C* **2020**, *124*, 8795−8805.

https://doi.org/10.1021/acs.jpcb.1c01737
J. Phys. Chem. B 2021, 125, 5160−5170